

Accelerated chemical space search using a quantum-inspired cluster expansion approach

Hitarth Choubisa^{*,1}, Jehad Abed^{*,1}, Douglas Mendoza^{2,3}, Zhenpeng Yao^{2,3,5}, Ziyun Wang^{1,4}, Brandon Sutherland¹, Alán Aspuru-Guzik^{5,6,7,8,†}, Edward H Sargent^{1, †}

¹Department of Electrical and Computer Engineering, University of Toronto, 10 King's College Road, Toronto, ON, M5S 3G4, Canada.

²Department of Chemistry, University of Toronto, 80 St. George Street, Toronto, ON M5S 3H6, Canada

³Department of Chemistry and Chemical Biology, Harvard University, 12 Oxford Street, Cambridge, MA 02138, USA

⁴School of Chemical Sciences, The University of Auckland, Auckland, 1010, New Zealand

⁵Chemical Physics Theory Group, Department of Chemistry, University of Toronto, Toronto, ON M5S 3H6, Canada

⁶Department of Computer Science, University of Toronto, Toronto, ON M5S 3H6, Canada

⁷Vector Institute for Artificial Intelligence, Toronto, ON M5S 1M1, Canada

⁸Lebovic Fellow, Canadian Institute for Advanced Research, Toronto ON, M5S 1M1, Canada

(*) These authors contributed equally to this work.

(†) Correspondence and requests for materials should be addressed to Alán Aspuru-Guzik (alan@aspuru.com) and Edward H. Sargent (ted.sargent@utoronto.ca)

Abstract:

To enable the accelerated discovery of materials with desirable properties, it is critical to develop accurate and efficient search algorithms. Quantum annealers and similar quantum-inspired optimizers have the potential to provide accelerated computation for certain combinatorial optimization challenges. However, they have not been exploited for materials discovery due to absence of compatible optimization mapping methods. Here we show that by combining cluster expansion with a quantum-inspired superposition technique, we can lever quantum annealers in chemical space exploration for the first time. This approach enables us to accelerate the search of materials with desirable properties 20 times faster over the Metropolis algorithm, with an increase in acceleration factor up to 150 for large systems. Levering this, we search chemical space and find a promising previously unexplored chemical family of Ru-Cr-Mn-Sb-O₂. The best catalyst in this chemical family show a mass activity 8 times higher than state-of-art RuO₂ and maintain performance for 180 hours while operating at 10mA/cm² in acidic 0.5 M H₂SO₄ electrolyte.

Introduction:

Finding materials with desirable properties such as high d-band centers, high stability, high mobilities, optimal bandgaps, or low overpotentials to enable efficient energy harvesting¹, catalysis², light emission³, sensing⁴, and more is a challenging high-order optimization problem. Traditionally, density functional theory (DFT) based screenings^{5,6} have been used to explore chemical space. However, the high computational cost associated with DFT calculations⁷ and the vastness of chemical space⁸ make exhaustive searches infeasible. To more rapidly predict material properties, studies in recent years have employed machine learning (ML) based surrogate models⁹⁻¹³. While such models circumvent the high computational cost associated with DFT, they do not offer a solution to the effective exploration of chemical space as they require a rate-limiting DFT-optimized geometry as the predictor¹⁴.

Recent studies proposed generative models (GMs) such as variational autoencoders (VAEs)^{7,14–16} and generative adversarial networks (GANs)^{17–20} to accurately predict properties without DFT relaxation. However, chemical exploration using GMs can be limited due to the generation of infeasible structures, absence of efficient search strategies and more. Therefore, ensuring global optimization across an exhaustive search within chemical space is difficult with such methods. This is further complicated by the observation that formulating the chemical space search as an optimization problem is itself challenging due to the absence of a simple analytic optimization expression and the non-convex nature of structure-property relationships due to the presence of multiple local minima^{21,22}.

We aim to address the above challenges by developing a new method to search chemical space by reframing the problem as one of finding the Ising Hamiltonian's ground state (**Figure 1**). Our method maps the Cluster Expansion (CE)^{23,24} formulation to an Ising model. This mapping enables potential use of quantum annealers and QUBO solvers to perform rapid global searches in chemical space. We choose a quantum-inspired optimization engine (Digital Annealer²⁵; henceforth referred to as DA; refer to Methods subsection on DA for more details) as the choice to solve for the ground state of our Ising model. Our choice is inspired by the fact that DA has been shown to efficiently find ground states of Ising models^{26,27}. We term the approach **QCE (Quantum-inspired Cluster Expansion)**. QCE not only allows us to circumvent the DFT relaxation process and makes property predictions computationally inexpensive but also enables us to accelerate the search for materials that optimize target properties of interest (**Figure 1**).

In this paper we first detail the QCE method and benchmark it by finding stable materials in the quaternary Cu-Ni-Pd-Ag chemical system. Following the benchmark, we lever the framework to find stable and efficient acidic OER catalysts by developing an experimentally verified quantum mechanical catalyst efficiency proxy. Finally, we verify our predictions experimentally and our top catalyst (a never before reported multi-metal oxide) demonstrates best-in-class stability among all acidic rutile OER catalysts with overpotentials < 250 mV.

Mapping cluster expansion to Ising Hamiltonian instance:

Cluster expansions (CEs) are power series expansions of the partition function that account for many-body interactions and have been employed for exploration of materials^{24,28–32}. In CE, the desired property E is expressed as a function of configuration σ of a specific lattice,

$$E(\sigma) = \sum_f J_f \Pi_f(\sigma) \quad (1)$$

where J_f s are fitted correlation coefficients and $\Pi_f(\sigma)$ s are correlation functions composed of multi-body interaction terms where σ can be 0 or 1. Furthermore, correlation functions $\Pi_f(\sigma)$ s are functions of configuration σ as,

$$E(\sigma) = \sum_{i \in \text{cluster}_1} J_f \langle \Phi_i(\sigma_i) \rangle_f + \sum_{i,j \in \text{cluster}_2} J_f \langle \Phi_i(\sigma_i) \cdot \Phi_j(\sigma_j) \rangle_f \quad (2)$$
$$+ \sum_{i,j,k \in \text{cluster}_3} J_f \langle \Phi_i(\sigma_i) \cdot \Phi_j(\sigma_j) \cdot \Phi_k(\sigma_k) \rangle_f + \dots$$

where $\Phi_i(\sigma_i)$ is an orthogonal basis function dependent on the atom type σ_i occupying the corresponding site i ³¹. Terms cluster_1, cluster_2 and cluster_3 are unique combinations of sites that constitute single-body, 2-body, and 3-body interactions. Coefficients J_f s are obtained by fitting the CE on the data (initial structures and target properties) generated using ab-initio methods such as Density Functional Theory (DFT)^{32–34} (**Figure S1(B)**). The cluster expansion is an infinite series but in most cases, it can be approximated as a finite series^{34,35}.

The key step of QCE mapping is expressing the basis functions $\phi_i(\sigma_i)$ as linear combination of all possible basis functions for every site within the lattice:

$$\phi_i(\sigma_i) = \sum_{j=1}^n C(M_j) \cdot \phi_i(\sigma_i = M_j) \quad (3)$$

such that $M_j, j = 1 \dots n$ represent the set of elements being considered for the site i and

$$C(M_j) \in \{0,1\} \forall j$$

$$\sum_{j=1}^n C(M_j) = 1$$

Several candidate functions can be used for the encoding scheme $C(\cdot)$ (refer to Methods subsection Encoding schemes for QCE). Substituting for Φ_i from (3) in (2) yields an expression with several multi-body spin terms ($q_0q_1, q_0q_1q_2, q_0q_1q_3q_4, \dots$) where q_k is a binary variable representing 0 or 1 spin values. We use term reduction as reported by Babbush et al.³⁶ to simplify the expression repeatedly until a Quadratic Unconstrained Binary Optimization (QUBO) expression is obtained.

The QUBO expression is then transferred to DA for efficient search and finding configurations that have the minimum/maximum of the property that was expressed by the trained CE model (refer to Methods subsection on DA and cluster expansion training for more details). Since any QUBO expression can be mapped to an Ising Hamiltonian, our proposed approach can be used by any Ising model solver such as a quantum annealer for optimizing materials within chemical space. The complete process is summarized in **Figure 1**.

Benchmarking our approach through exploration of quaternary chemical space (Cu-Ni-Ag-Pd)

To benchmark the performance of our proposed approach, we explore the quaternary chemical space spanned by Cu-Ni-Ag-Pd in an FCC lattice due to their potential applications as fuel cell membranes³⁷ and oxygen reduction electrocatalysts³⁸. Stability of materials for such applications is critical and is being extensively investigated^{37,39}. Thus, finding stable alloys within this chemical space can be an exciting prospect^{37,40} (**Figure 2a**). We used DFT for data generation followed by training of a CE model to predict mixing energy (ΔH_{mix}) (refer to Methods subsection on data generation and mixing energy for more details) and use it a measure of alloy's stability against its single metal constituents. The

model achieves LOOCV (leave-one-out-cross-validation) MAE of 9 meV/atom (**Figure 2b**; methods subsection on cluster expansion training for more details).

Using the scheme presented in the previous section, we prepared the QUBO representation of our CE model and transferred it to the DA for finding structures with minimum mixing energy (refer to methods subsection on DA for more details). We obtained **Ag_{0.5}Pd_{0.5}** as composition with most negative ΔH_{mix} of -0.17 eV/atom (**Figure 2c**) exhibiting long range ordering (**Figure S2**). This observation aligns with our results obtained through semi-grandcanonical Metropolis Monte Carlo ensemble sampling.

To further explore the potential of our developed mapping, we sought to determine stable alloys within the Cu-Ni-Pd chemical subspace. We achieved this by restricting the possible values of the basis function Φ_i to only include relevant elements in the expansion of (3) (refers to methods subsection on Chemical subspace search for more details). Upon performing the search using DA, we obtained equimolar ordered **Cu_{0.5}Pd_{0.5}** alloy as the alloy with most negative mixing energy ($\Delta H_{mix} = -0.09$ eV/atom) in Cu-Ni-Pd space and therefore, stable (**Figure S3**). This observation is supported by a previous report about equimolar FCC Cu-Pd alloy being the more stable⁴⁰. We further compared the temporal performance of our approach to the Metropolis Monte Carlo algorithm in searching chemical space and observed an acceleration factor of 20 (refer to **Figure S4** for the detailed plot).

Finding stable and efficient OER materials

To demonstrate that the generalizability of our approach, we showcase the discovery of acidic oxygen evolution reaction (OER) catalysts^{41,42}. The development of OER catalysts has been the subject of significant research over the past few years^{39,43-48}. For the alkaline medium, several stable and efficient OER catalysts have been proposed; however, only a few stable, efficient, and cost-effective OER catalysts have been reported in literature for operation in an acidic medium^{44,49}.

High efficiency and high stability are two crucial requirements for a good OER catalyst. To develop a quantitative model for efficiency of the catalyst candidates, we built upon the d-band model by Hammer and Nørskov⁵⁰⁻⁵³ and recent studies about its interplay with p-band centers⁵⁴. We used materials and alloys constructed by substituting two different prototype structures: **ZrO₂** (P2₁/c; monoclinic) and **RuO₂** (P4₂/mnm; tetragonal) in our study (refer to Data Generation in Methods). Using logistic regression, we analyzed how the d-band center and p-band center determine the theoretical overpotentials (refer to logistic regression analysis in Methods; **Figure 3a**). We observe that probability of overpotential smaller than 350 mV is given by,

$$Prob(\eta < 0.35) = \frac{1}{1 + e^{\theta}} \quad (4)$$

$$where \theta = 0.72 \cdot p - 1.41 \cdot d$$

where η represent overpotential, p and d represent p-band center and d-band center respectively.

To further establish the validity of this theoretical analysis, we further conduct several in-lab experiments and demonstrate a coefficient of determination (R^2) of **0.71** in linking our analytical expression from **(7)** and experimental overpotentials for the catalysts with a p-value < 0.001 (refer to **SI note 3** and **Figures 3d, S6** for more details). We also report all the collected experimental quantities for the candidates with measurable activity and acidic stability in **SI note 4** as a tabular database for future machine learning explorations and for reference. In addition, we used mixing energy ΔH_{mix} to quantify stability of an alloy relative to its precursors.

Following the strategy for QCE, we trained CE models (refer to Methods subsection on **Chemical subspace search** for more details; **Figure S7**; methods subsection on cluster expansion training) and generated the QUBO representations for each of the three properties: $\Delta H_{mix}(H_E)$, p-band center (H_p) and d-band center (H_d) using QCE. The accuracy and performance of each of these models on validation data are shown in **Figures 3b, 3c, and 3d**. We defined QUBO for efficiency as,

$$H_{eff} = 0.72H_p - 1.41H_d$$

Thus, the problem of finding an efficient and stable OER catalyst transforms into finding a state that minimizes both H_{eff} and H_{stable} . We solve this problem by using a heuristic approach of optimizing the linear combination of the two QUBOs:

$$H_{mixed} = \lambda_1 H_{stable} + \lambda_2 H_{eff} \quad (5)$$

where $\lambda_1, \lambda_2 \in [0, \infty)$ (Refer to **Figure S8** for the effect of parameter λ). Transferring H_{mixed} represented as QUBO to DA and performing the optimization result in candidates that have promising stability as well as efficiency.

We search for different chemical subspaces within the two prototype structures by varying the relative weight parameter λ and chemical subspace of interest (**Figure S10** for details) while adding constraints to ratios of different elements. Based on our experiments, we find that $\lambda_1 = 0$ or $\lambda_2 = 0$ leads to catalyst candidates that are either unstable or inactive (Refer to **figure 4** for a summary of candidates experimentally tested and **table S1** for a detailed list) whereas non-zero pair lead to a balanced trade-off between stability and efficiency (**Figure S9**). We also compare this approach to a sequential search (search for stability followed by efficiency). We find that our heuristic approach outperforms a sequential search strategy (**SI note 6**).

Experimental verification:

All of the 49 electrocatalyst candidates in **Table S1** were synthesized using sol-gel synthesis followed by annealing in air for 2 hours⁵⁵. We observed that some compositions (8 compounds) were not successfully synthesized using the sol-gel method due to poor promotion of networks in the gel (**Figure 4a**). The crystal structure of the synthesized samples was screened using X-ray diffraction (XRD). XRD patterns were collected and classified into two groups: pure rutile phase (21 compounds) and multiple phases groups (20 compounds). One XRD pattern is shown in **Figure 4e** for

$\text{Ru}_{0.58}\text{Cr}_{0.25}\text{Mn}_{0.08}\text{Sb}_{0.08}\text{O}_2$ (R14-M10-46) showing characteristic peaks of a rutile structure similar to a baseline RuO_2 catalyst. The XRD peaks are broad indicating that our synthesis approach produced nanocrystalline electrocatalysts. Further analysis of the structure for all electrocatalysts is provided in **Table S2**. High-resolution transmission electron microscopy (HR-TEM) and scanning transmission electron microscopy (STEM) are shown for three samples in **Figure S10**. The nanoparticles have an average particle size of *ca.* 10 nm with a spherical shape suitable for electrocatalytic applications. The energy X-ray dispersive spectroscopy (EDS) elemental mapping shows a homogeneous distribution of elements in the three samples (**Figure S11**). The EDS elemental mapping of $\text{Ru}_{0.58}\text{Cr}_{0.25}\text{Mn}_{0.08}\text{Sb}_{0.08}\text{O}_2$ (R14-M10-46) matches within 5% error with the nominal composition of the compound (Ru: 59 ± 5.9 at. %, Cr: 20 ± 1.0 at. %, Mn: 9 ± 0.6 at. %, Sb 13 ± 3.4 at. % of the total metal amount). The electron diffraction rings of the three samples confirm the formation of a strained rutile structure (**Figure S12**).

The electrocatalysts were then drop-casted on carbon paper to screen the electrochemical performance. The overpotential of the electrocatalysts was measured in a three-electrode cell using 0.5M H_2SO_4 (**Figure 4b**, **Table S3**). The experimental overpotentials matched well with the trend of predicted activity (**Figure 3d**, **SI note 3**). We observe a coefficient of determination of 0.71 between our theoretically derived quantum mechanical proxy and in-lab experimental overpotential of catalyst candidates (*p-value* < 0.001). We use the structures as obtained by optimization of (5) to model every chemical composition. Furthermore, to compare the intrinsic activity of the electrocatalysts, we decouple the morphology effect from the activity by normalizing the current density by the active electrochemical surface area (ESCA) overpotential instead of the geometric area (**Figure 4c**, **Figure S13**). We then calculate the mass activity of the electrocatalysts normalized by the Ru amount in the electrocatalyst (**Figure 4d**). Taking into consideration both measures, we identified $\text{Ru}_{0.58}\text{Cr}_{0.25}\text{Mn}_{0.09}\text{Sb}_{0.08}\text{O}_2$ as the most promising candidate with the highest mass activity $381 \text{ A/g}_{\text{Ru}}$ (*ca.* 8 times higher than RuO_2) and a much lower overpotential increase rate of $2 \text{ mV}\cdot\text{hr}^{-1}$, 10 times slower

than RuO₂ (inset in Figure 4g, Table S3).⁵⁶ To better assess the stability of the electrocatalyst, we prepared it by spraying the electrocatalyst on carbon paper instead of drop-casting, the technique we used for screening purposes, to ensure a higher penetration of the particles through the hydrophilic carbon paper yielding in higher surface coverage and better mechanical attachment to the carbon fibers. We maintained the loading of the electrocatalyst between both preparation techniques at 1 mg/cm². Our candidate maintained an overpotential of less than 300 mV for 180 hours at a low overpotential increase rate of 2 mV/hr, 10 times lower than RuO₂ and any previous reports of rutile structure based catalysts³⁹. Finally, we also search existing databases (OQMD, AFLOW, Materials Project, OCP, ICSD) and literature for similar alloys and we were unable to find even a similar oxide compound with Ru, Cr, Mn and Sb present together. Our QCE method was therefore able to effectively search chemical space, identify a new promising family of multi-metal oxides for exploration and discover a highly efficient and stable OER catalyst.

Origins of the catalyst stability and efficiency:

To better understand the cause of higher activity and stability of our top catalyst candidate: Ru_{0.58}Cr_{0.25}Mn_{0.09}Sb_{0.08}O₂ (henceforth referred to as catalyst RuCrSbMnO₂), we performed detailed DFT calculations and analysis. We used the crystal structure for each candidate, as obtained by minimizing the joint Hamiltonian in (5), for performing the following analysis (Figure S14 for crystal structure of RuCrMnSbO₂). Bader charge analysis showed that the average partial charge on Ru increased from **1.73|e|** in pure RuO₂ to **1.82|e|** in RuCrMnSbO₂. Ru with a higher partial charge indicates improved ability of the catalyst to oxidize water to oxygen i.e., OER. Additionally, to explore the origin of the stability of the catalyst candidates, we further analyzed the density of states (DOS). As shown in Figure 5 (a, b) incorporation of Cr, Mn and Sb alter the DOS of RuO₂, causing occupation at Fermi level to decrease from **38 states/spin** to **18 states/spin**. This decrease in DOS at fermi energy indicates stronger bonding between metal atoms, leading to stabilization of our solid solution^{39,57} (Figure S15 for a

comparison study that considers only Cr and Mn). Table 1 summarizes our observations against previously reported $\text{Ru}_{0.4}\text{Cr}_{0.6}\text{O}_2$ and RuO_2 ³⁹. We also observe that entropic contributions further stabilize the predicted composition RuCrMnSbO_2 as compared to previously reported RuO_2 and $\text{Ru}_{0.4}\text{Cr}_{0.6}\text{O}_2$. These observations align with our observed experimental measurements of 180 hours stability for RuCrMnSbO_2 as compared to unstable RuCrO_2 and 40 hours stability of pure RuO_2 (catalyst ID *R8-M16-16* and RuO_2 for detailed experimental results on stability and activity in SI tables 1-3).

Compound	ΔH_{mix} (eV/atom)	Bader charge on Ru	DOS at E_{fermi} (states/spin)	Entropy contribution at 550° C (eV/atom)
RuCrMnSbO_2	-0.08	1.82	18	-0.078
RuCrO_2	-0.05	1.92	19	-0.048
RuO_2	0.0	1.73	38	0.000

Table 1: Comparison of different stability contributing factors for RuO_2 , $\text{Ru}_{0.4}\text{Cr}_{0.6}\text{O}_2$ and RuCrMnSbO_2

At the same time, we calculated free energy profiles (ΔG) of OER to compare the activities of RuCrMnSbO_2 to RuO_2 (refer to Data Generation in Methods for details and SI Note 6). As can be seen from **Figure 5 (c, d)**, the formation of OOH was found to be the rate-determining step. For our catalyst, the free energy change was found to be 1.92 eV which is smaller than the free energy change corresponding to RuO_2 (2.02 eV) and consistent with the experimental observation of smaller overpotentials.

Conclusion:

In this study, we reported a new approach for materials discovery that maps the chemical space search problem to one of finding the ground state of the Ising Hamiltonian. This enables us to use a quantum-inspired computing framework to find materials with optimal properties in an accelerated and efficient fashion, 20 times faster than the Metropolis algorithm. Our efforts led us to develop an improved efficiency proxy and discover a stable and efficient OER catalyst **$\text{Ru}_{0.58}\text{Cr}_{0.25}\text{Mn}_{0.09}\text{Sb}_{0.08}\text{O}_2$** . Post-hoc DFT analysis further explains the electronic origins of the stability and efficiency of the catalysts.

However, we should also take note of one of the limitations of the current study: restriction of one lattice across the chemical space, which is not what is always desired in materials discovery pipelines. Nevertheless, this can be handled by using extended cluster expansion mapping as proposed by Koretaka Yuge⁵⁸. We plan to incorporate this as part of our future work.

Methods:

Digital Annealer (DA):

Fujitsu's Digital Annealer (DA) is designed to efficiently solve combinatorial optimization problems²⁵ formulated as fully connected Ising problems expressed in Quadratic Unconstrained Binary Optimization (QUBO) form. In most general case, a QUBO can be represented as: $F(q_0, q_1, \dots, q_n) = \sum_{ij} a_{ij} q_i q_j$ where q_i ($i = 1 \dots n$) are binary variables.

In this work, we used third-generation DA that can handle up to 100k binary decision variables. Given a QUBO expression, the DA finds the assignment of binary variables (referred by q_0, q_1, \dots) such that the expression value is minimized. All experiments were conducted on the DA environment prepared for research use.

Data generation:

We use RuO₂ (Materials Project⁵⁹ ID: mp-825) and ZrO₂ (Materials Project ID: mp-2858) as the prototype structures and generated 72 and 96 atoms supercells respectively for training the cluster expansion models. 120 randomly substituted alloy structures were generated for each of the chemical spaces spanned by Ru-Ti-W-Sb-Cr-Mn-V-Co and Ru-Zr-Hf-Y-V-Co-Fe-Ce using Clusterx^{60,61} respectively. We further randomly selected half of the 240 structures and generated surfaces with 110 orientation for the calculation of adsorption energies with vacuum spacing of 10Å. DFT calculations were performed in VASP for the bulk and surface structures using Perdew-Burke-Ernzerhof⁶² (PBE) exchange-correlation functional augmented with Hubbard Coulomb interaction potential (U) corrections for d-electrons taken

from Materials Project⁵⁹. Valance electrons were described with a 520-eV plane-wave basis set and 0.05 eV Gaussian smearing of the electronic density. All the geometries were optimized with the energy convergence criterion of 10^{-4} eV and force convergence of 10^{-3} eV/Å. Core electrons were described using the projector augmented wave (PAW) method. All the calculations were spin-polarized and reciprocal space was simulated using 1x1x1 k-point mesh centered at gamma.

For Cu-Pd-Ni-Ag chemical space benchmark, we used Cu-FCC 64 atoms supercell as the prototype structure. 120 randomly decorated structures were generated. DFT calculations were performed in VASP for the bulk using Perdew-Burke-Ernzerhof⁶² (PBE) exchange-correlation functional. Valance electrons were described with a 520-eV plane-wave basis set and 0.05 eV Gaussian smearing of the electronic density. All the geometries were optimized with the energy convergence criterion of 10^{-4} eV and force convergence of 10^{-3} eV/Å. Core electrons were described using the projector augmented wave (PAW) method.

To perform post-hoc DFT analysis of the RuCrMnO₂ and RuCrMnSbO₂, we generate surfaces with orientations: [001, 100, 101, 110] and choose 110 as the orientation to perform adsorption energy calculations due to lower surface energy. The post-hoc DFT analysis was done on a denser Monkhorst k-points grid 2x2x2 to improve the accuracy. The rest of the parameters stayed the same as in the preceding paragraph.

Mixing energy (ΔH_{mix}):

We define mixing energy or enthalpy of mixing ΔH_{mix} as excess energy with respect to the single metal precursors. For metal alloys it assumes the form:

$$\Delta H_{mix}(A_x B_y C_z D_w) = E(A_x B_y C_z D_w) - \frac{x \cdot E(A_u) + y \cdot E(B_u) + z \cdot E(C_u) + w \cdot E(D_w)}{u}$$

where $u = x + y + z + w$ and $E(\cdot)$ represents total energy of the concerned phase.

Similarly, for mixed metal oxides, it assumes the form:

$$\Delta H_{mix}(A_x B_y C_z D_w O_v) = E(A_x B_y C_z D_w O_v) - \frac{x \cdot E(A_u O_v) + y \cdot E(B_u O_v) + z \cdot E(C_u O_v) + w \cdot E(D_w O_v)}{u}$$

where $u = x + y + z + w$.

Cluster expansion training:

We used ClusterX package of CELL to train cluster expansion models. The scripts and codes used are part of the submission package. We tested different cluster generation schemes by tuning the kind of interactions and cut-off for each of the interactions (refer to SI figure 10 for a comparison plot). Parameters that lead to lowest cross-validation error were chosen for analysis.

We end up with a two-body interaction CE model with cutoff radius of 4A for FCC Cu-Ni-Pd-Ag chemical system. For Ru-Ti-W-Sb-Cr-Mn-V-Co and Ru-Zr-Hf-Y-V-Co-Fe-Ce chemical systems, we get an optimal cluster expansion that has both 2 body and 3 body interaction terms with a cutoff of 5A each for prediction of mixing energies. We use 2-body interaction cluster expansions for d-band and p-band predictions, both with cutoff radius of 4A.

Encoding schemes for QCE:

Several candidate functions can be used for the encoding scheme $\mathcal{C}(\cdot)$. Two natural choices are:

- Encoding 1:

$$\Phi_i(\sigma_i) = \sum_{j=1}^n q_j \cdot \phi_i(\sigma_i = M_j)$$

where q_j are binary decision variables and the second one-hot constraint is then enforced as a penalty:

$$P_i(\sigma_i) = \left(\sum_{i=1}^n q_i - 1 \right)^2$$

- Encoding 2:

$$\Phi_i(\sigma_i) = \sum_{j=1}^n f_j(q_1, q_2, \dots, q_k) \cdot \phi_i(\sigma_i = M_j)$$

where q_j are binary decision variables, $k = \text{ceil}(\log_2 n)$ where n is total number of element types.

Functions $f_j(\cdot)$'s are defined such that $f_j(\cdot)$ is non-zero only for one specific configuration $\vec{q} \in \{0,1\}^k$. This is possible since k binary variables can be used to uniquely represent 2^k possibilities. To construct f_j using this encoding scheme, one would enumerate all possible bit strings in the space $\{0,1\}^k$ and then construct polynomials for each of them. For example, f_j 's would be $(1 - q_1)(1 - q_2)$, $q_1(1 - q_2)$, $(1 - q_1)q_2$ and q_1q_2 for representing a 4 elements system.

Chemical subspace search:

For performing QCE, we know from equation (3) that we rewrite the cluster expansion formulation as,

$$\Phi_i(\sigma_i) = \sum_{j=1}^n C(M_j) \cdot \phi_i(\sigma_i = M_j)$$

such that $M_j, j = 1 \dots n$ represent the set of elements being considered for the site i and

$$C(M_j) \in \{0,1\} \forall j$$

$$\sum_{j=1}^n C(M_j) = 1$$

In order to restrict the sampling to a set of elements, we limit the summation to set of elements of interest to us. If one wants to avoid element M_s , one can rewrite the summation as,

$$\Phi_i(\sigma_i) = \sum_{j=1, j \neq s}^n C(M_j) \cdot \phi_i(\sigma_i = M_j)$$

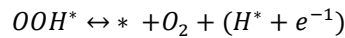
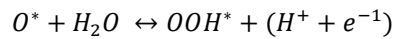
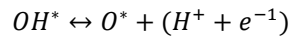
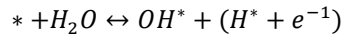
Such that

$$C(M_j) \in \{0,1\} \forall j$$

$$\sum_{j=1}^n C(M_j) = 1$$

OER reaction mechanism:

OER in acidic and neutral medium is a 4-step reaction with the following reaction mechanism^{39,44,45}:



where * denotes the species adsorbed at the catalyst surface.

The theoretical overpotential (η_{OER}) is thus defined as,

$$\eta_{OER} = \max \frac{(\Delta G_7, \Delta G_8, \Delta G_9, \Delta G_{10})}{e} - 1.23 \text{ V}$$

$$= \frac{\max(\Delta G_{OH^*}, \Delta G_{O^*} - \Delta G_{OH^*}, \Delta G_{OOH^*} - \Delta G_{O^*}, 4.92 - \Delta G_{OOH^*})}{e} - 1.23 \text{ V}$$

Calculation of η_{OER} , thus, requires values of adsorption energies for reaction intermediates O , OH and OOH . These DFT energy calculations are computationally expensive. Usually, scaling relationships are used to reduce the number of calculations needed⁴¹. However, scaling relationships break down in the case of alloys (**Figure S3**).

Calculation of band centers:

D-band model relates the surface reactivity with the shifts in the d-band center of the catalyst where the d-band center is a single state with energy ϵ_d that approximates the interaction of participating bands of d-states. In particular, we calculated d-band centers and p-band centers using the first moments as,

$$\epsilon_{M-d} = \frac{\int_{-\infty}^{\infty} E D_{M-d}(E - E_F) dE}{\int_{-\infty}^{\infty} D_{M-d}(E - E_F) dE} \quad (8)$$

$$\epsilon_{M-p} = \frac{\int_{-\infty}^{\infty} E D_{M-p}(E - E_F) dE}{\int_{-\infty}^{\infty} D_{M-p}(E - E_F) dE} \quad (9)$$

where M is the corresponding element and D_{M-y} represents partial DOS of orbital y of element M in the system.

Logistic Regression Analysis for efficiency:

We used logistic regression, as implemented in scikit-learn, to investigate the relationship between band centers and overpotentials of the materials. We first calculated theoretical overpotentials (OER reaction mechanism subsection of Methods) of 60 randomly chosen candidate materials from the two chemical families under consideration (Data generation subsection of Methods).

Irrespective of the threshold set for distinguishing low and high overpotentials, our logistic regression model achieved a 5-fold CV f1-score in the range (0.90 – 0.92). We tried 5 regularly spaced points between 0.35 V to 0.5 V as the thresholds. This number is supported by a recent study by Back et al⁴⁵ where 0.5V was used as the cut-off overpotential for identifying promising OER catalysts. We represent this observation in **Figure 3a** where we can see a clustering of “good” catalysts. The logistic regression equation for threshold 0.35 has the following equation:

$$Prob(\eta < 0.35) = \frac{1}{1 + e^{\theta}} \quad (7)$$

$$\text{where } \theta = 0.72 \cdot p - 1.41 \cdot d$$

where $P(\eta < 0.35)$ denotes the probability of a catalyst with overpotential less than 0.35V, p indicates the p-band center and d indicates the d-band center of the catalyst in consideration, respectively. Furthermore, refer to **Figure S7** to analyze the variation in intermediate adsorption energies as a function of band centers.

Materials:

Metal precursors including ruthenium chloride hydrate, ($\text{RuCl}_3 \cdot x\text{H}_2\text{O}$), chromium (iii) chloride anhydrous, 99.99% trace metals basis (CrCl_2), manganese chloride (MnCl_2), tungsten (VI) chloride (WCl_6), titanium diisopropoxide bis(acetylacetonate), 75wt. % in isopropanol, Vanadium(iii) chloride (VCl_3), and Propylene oxide ($\geq 99.5\%$ GC) were all purchased from Sigma-Aldrich. Nafion[®] (5 wt% in a mixture of lower aliphatic alcohols and water) and AvCarb MGL190 were used for electrode preparation. All chemicals were used without any further purification.

Experimental synthesis:

The mixed metal oxides were synthesized using a modified sol-gel procedure⁶³ by completely dissolving a total amount of 2.7 mmol of the metal precursor mixture in 3.5 mL anhydrous ethanol. The solution was vortexed for 5 mins and sonicated in a water bath for 1 hour until it is clear. Then, it was chilled in a refrigerator for 2 hours to prevent any undesired hydrolysis and condensation which may affect the gelation process. Afterward, a magnetic stirrer was used to mix the solution vigorously while 2 mL of propylene oxide was added dropwise to the mixture. The solution was aged for 1 day to promote gel formation and then washed with acetone; the process was repeated for 5 days before drying the gel in a vacuum oven for 1 day. The sol-gel process produces amorphous oxides, therefore, to produce a rutile crystal structure the dried powder was annealed at 400°C for 2 hours.

For the fast electrochemical purpose, the working electrode was prepared on 0.5 cm x 0.5 cm untreated carbon paper (AvCarb MGL190) by drop casting. First, a catalyst ink was prepared by mixing 10 mg of the catalyst in 1 mL mixture of water and ethanol (4:1, v/v). Then, the ink was sonicated in an ice bath for 1 hour. Finally, a 25 μ L drop of the ink was deposited on the carbon paper and allowed to dry in the air. For final electrochemical testing, the working electrode was prepared by spraying the electrocatalyst using N₂ on 0.5 cm x 0.5 cm untreated carbon paper. The ink was prepared by mixing 10 mg of the catalyst in 1 mL of isopropanol. Then, the ink solution was sonicated in ice bath for 1 hour before spraying it on the carbon paper on the hot plate at 90 °C.

Electrochemical testing

Electrochemical testing was conducted in a three-electrode setup using a Hg/Hg₂SO₄ as the reference electrode and graphite rod as the counter electrode. The OER activity was evaluated by running linear sweep voltammetry (LSV) with a rate of 5 mV/s. The stability of the catalyst was evaluated by conducting chronopotentiometry at 10 mA/cm².

All potentials were iR-corrected by measuring the solution resistance from electrochemical impedance spectroscopy (EIS) with a bias of 1.53V vs. RHE in the frequency range from 100 kHz to 10 MHz and an amplitude of 5 mV. All the potentials in this study were reported with respect to a reversible hydrogen electrode (RHE) using the following relationship:

$$E_{RHE} = E_{Hg/Hg_2SO_4} + 0.640 + 0.0591 \times pH$$

Structure analysis

The crystal structure of catalysts was determined using X-ray Diffraction (XRD). A Miniflex 600 (Rigaku, Japan) equipped with D/tex Ultra silicon trip detector and Cu K α radiation ($\lambda = 1.5418 \text{ \AA}$) was used. Powders were prepared by mixing with acetone and then dropping a small drop of the mixture to fill a 4

mm diameter x 100 μm deep groove in a single crystal silicon holder (zero-background). The angle was varied between 20° to 80° with a step size of 0.005° and a scan rate of 1 deg/min.

To evaluate the nanocrystalline size and macrostrain of the electrocatalysts, we used Scherrer's equation and microstrain equation:

$$D = \frac{K\lambda}{FWHM \cos \theta}, \text{ Scherrer's equation}$$

$$\varepsilon = \frac{FWHM}{4 \tan \theta}, \text{ microstrain}$$

D is the mean crystallite size, λ is 0.154 nm for Cu X-ray source, K is shape factor has a typical value between 0.9-1. The full-width half-maximum (FWHM) of the peaks were measured by fitting to Gaussian distribution and then calculated from the standard deviation (σ) using the following relation:

$$FWHM = 2\sqrt{2 \cdot \ln 2} \approx 2.355 \sigma$$

Electron microscopy

The structural characterization and elemental mapping of the catalysts were done using High Resolution Scanning Electron Microscopy (HRSEM) and Transmission Electron Microscope (TEM). The experiments were conducted in a Hitachi HF3300 equipped with a cold field emission electron gun using an accelerating voltage of 300 kV. Energy X-ray dispersive spectroscopy (EDS) detector was used in scanning transmission electron microscopy (STEM) mode to analyze and quantify the composition of the nanoparticles. Also, a secondary electron (SE) detector was used to collect HRSEM images of the nanoparticles. Powder samples were prepared in ethanol and sonicated for 10 minutes before drop casting a 1-2 μL drop on a 400-mesh copper grid and drying overnight.

Data and Code Availability:

All the data supporting this study are available with the article's Supplementary Information (SI).
Code used is also available in the SI. Please refer to SI note 6 for the code organization.

Figures:

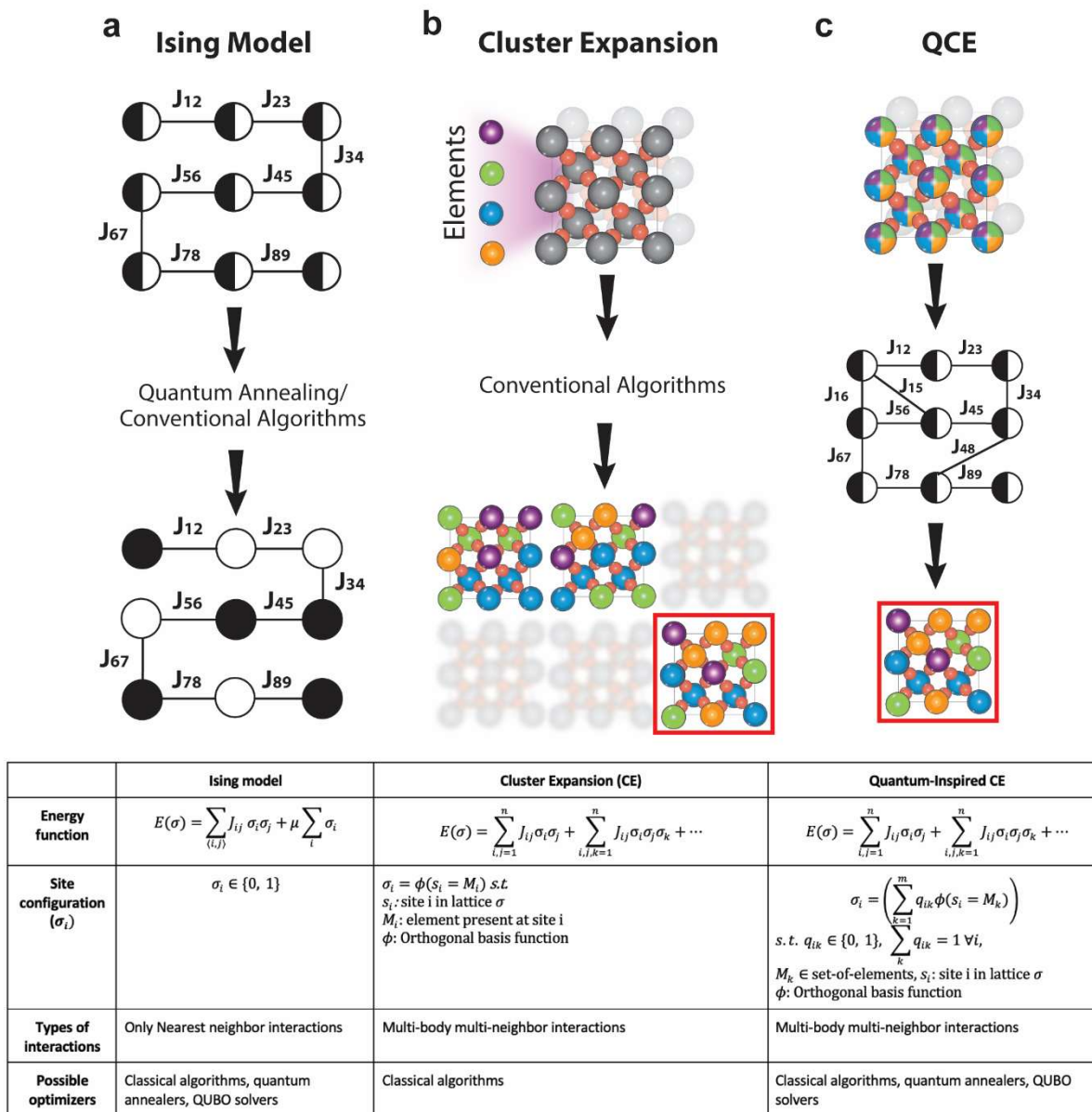


Fig. 1: Mapping chemical space search to finding the ground state of an Ising model with Quantum-Inspired Cluster Expansion (QCE)

Figure shows and compares the Ising model (1st column), cluster expansion (2nd column) and our proposed approach (3rd column). Ising models are computational models of ferroelectricity. Various optimizers including quantum annealers, quantum-inspired optimizers as well as conventional algorithms such as Metropolis can be used to find ground state of Ising models. On the other hand, Cluster expansions (CE) are used for solving the combinatorial search problem in chemical space but only conventional algorithms have been used so far for exploring CE. As part of this paper, we propose a mapping (3rd column of inset table) from CE to an Ising model. This enables us to lever same set of optimizers for CE as those are available for finding ground state of Ising models.

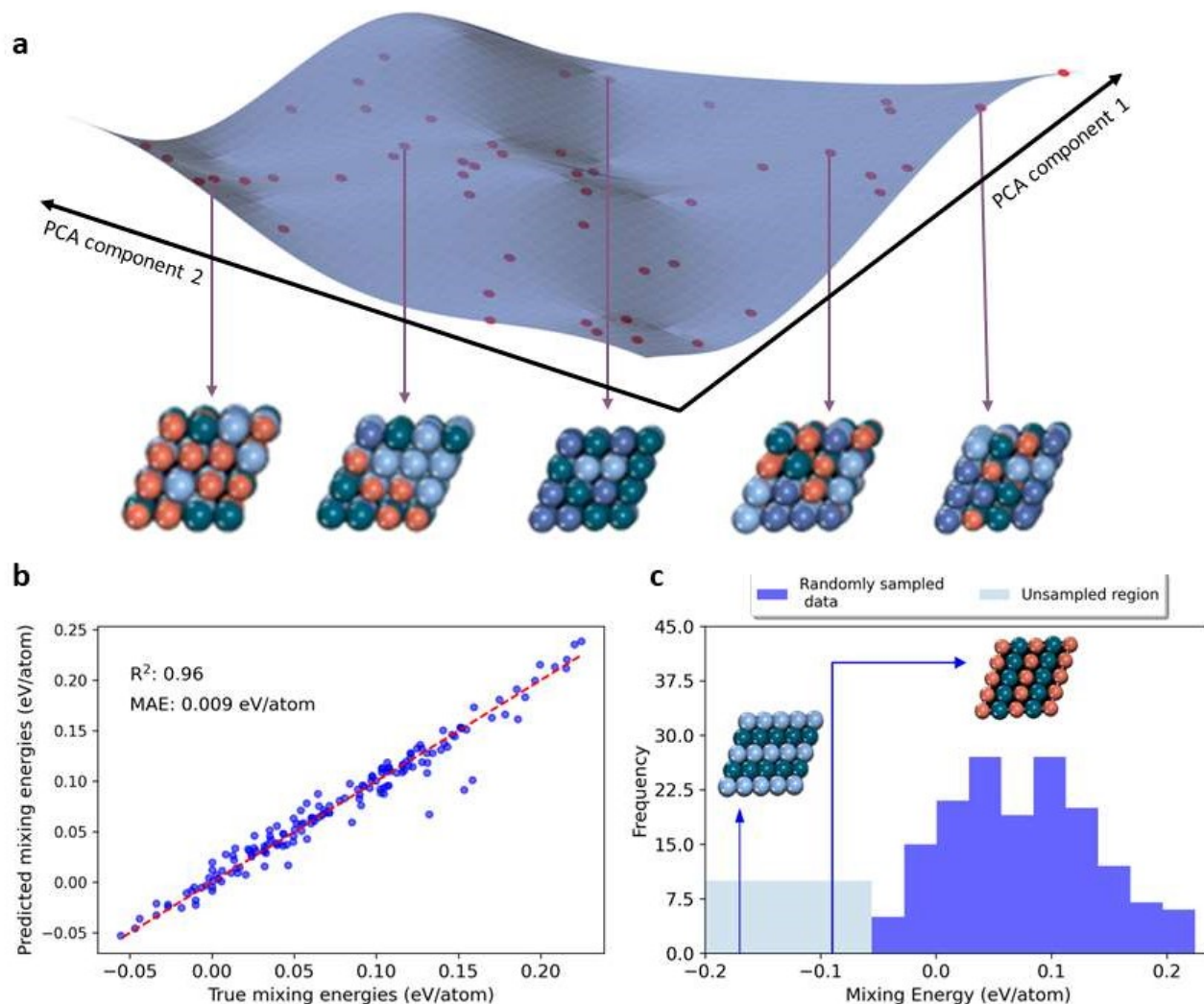


Fig. 2: Chemical space exploration using proposed mapping

Exploring chemical space with random sampling often ends up with limited exploration. Accurate surrogate models and search algorithms can help us explore unsampled chemical territories. (a) Shows the energy above hull landscape in a 2D projection of the chemical space. Red dots correspond to the sampled points and each of the points in this 2D projection correspond to a chemical structure. As we can see the global minima has not been sampled. (b) Cluster expansion predictive accuracy for quaternary alloy composed of Cu-Ni-Pd-Ag (our benchmark materials system). (c) Distribution of mixing energies for our training dataset and results of exploration with the annealer in finding stable compositions. The inset crystals are the result of search conducted on the annealer: chemical ternary subspace search yielded equimolar Cu-Pd as the most stable alloy whereas Quaternary Chemical space search yielded a Pd-Ag composition as one of the stable alloys.

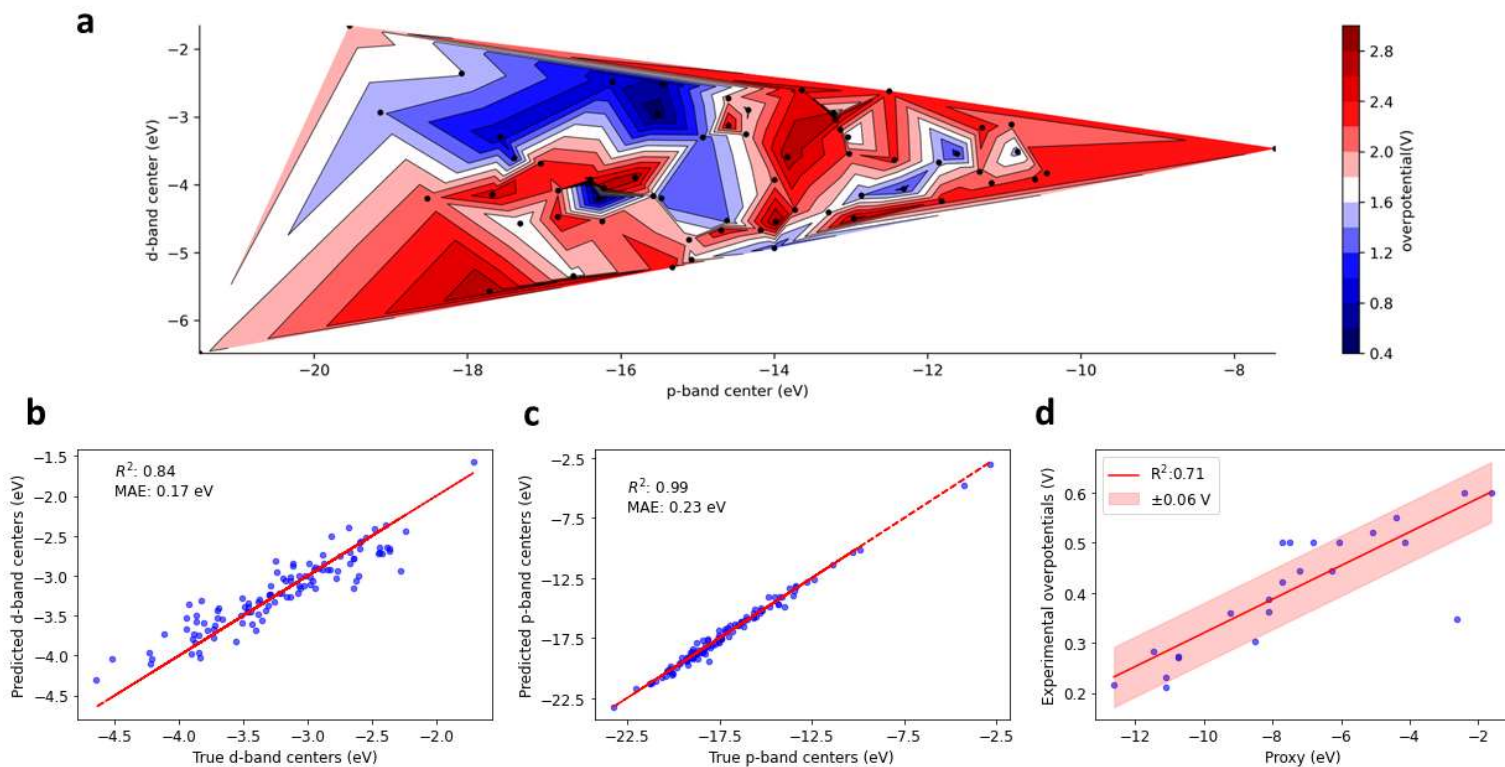


Fig. 3: Development of an efficiency proxy for OER catalysts and training the cluster expansions.

Investigation of the relationship between theoretical overpotentials and bulk p and d band centers. (a) shows overpotential contours as a function of d and p band centers with clustering around points; (b) Cluster expansion model accuracy for the prediction of p-band centers; (c) Cluster expansion predictions for d-band centers with its performance; (d) comparison of our theoretical efficiency proxy and experimental overpotentials obtained in lab

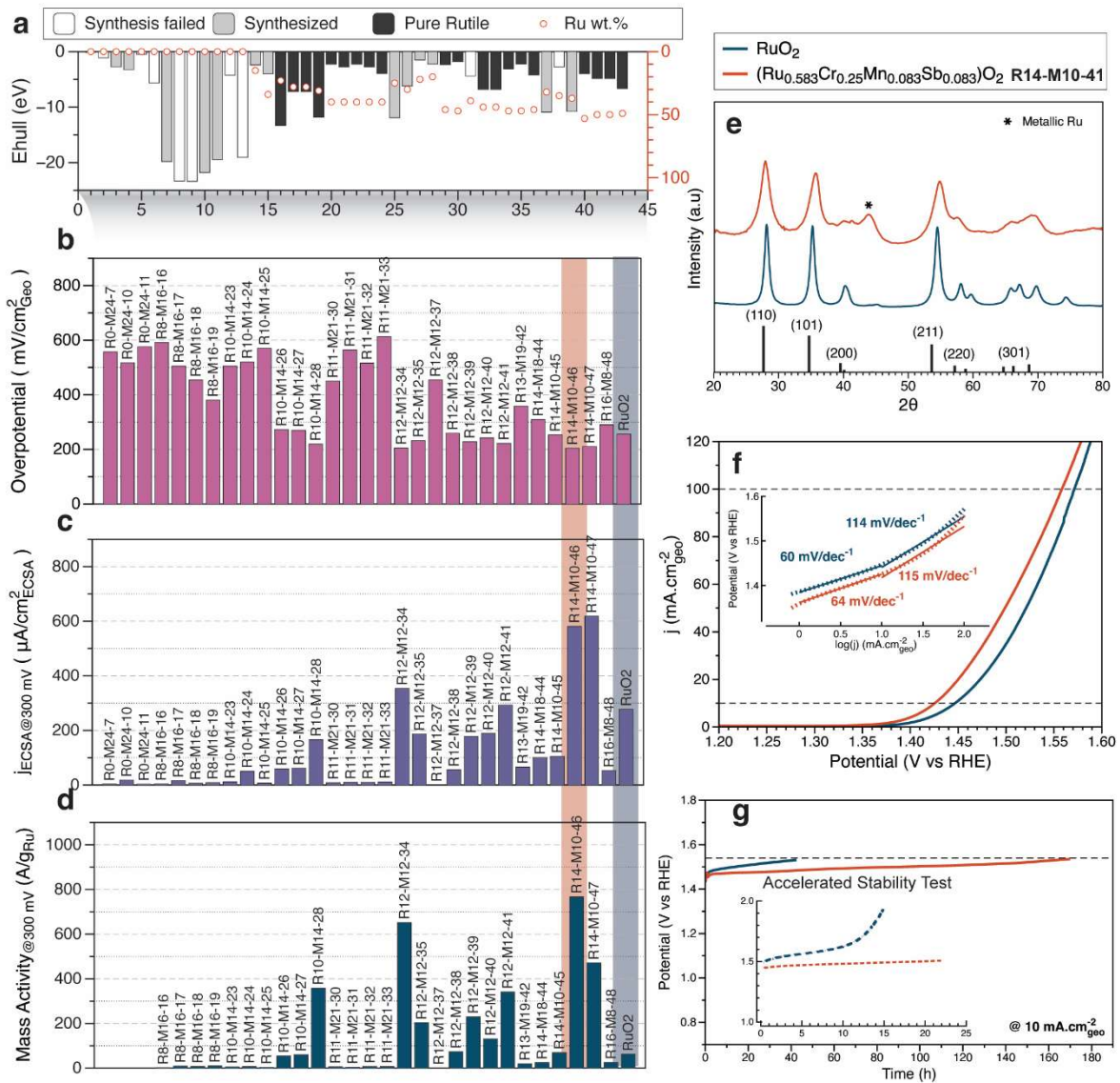


Fig. 4: Experimental screening of electrocatalysts.

(a) The hull energy of all electrocatalyst candidates considered for experiments in this study. The candidates were classified based on the synthesis outcome: synthesis failed (the electrocatalyst wasn't produced), synthesized, and pure Rutile phase. (b) Overpotential screening of synthesized electrocatalysts. (c) The intrinsic activity of electrocatalysts normalized by the electrochemical surface area. (d) The mass activity of electrocatalysts normalized by the total mass of Ru. (e) XRD and (f) polarization curves (Tafel slope analysis in the inset) of the best electrocatalyst candidate R14-M10-41 ($\text{Ru}_{0.58}\text{Cr}_{0.25}\text{Mn}_{0.083}\text{Sb}_{0.083}\text{O}_2$) and a baseline RuO_2 catalyst. (g) Chronopotentiometry test of the electrocatalysts sprayed on carbon paper electrodes. In the inset is the accelerated test conducted on the electrocatalysts drop-casted on carbon paper. The electrocatalyst loading for all samples is 1 mg/cm². The electrolyte is 0.5 M H₂SO₄.

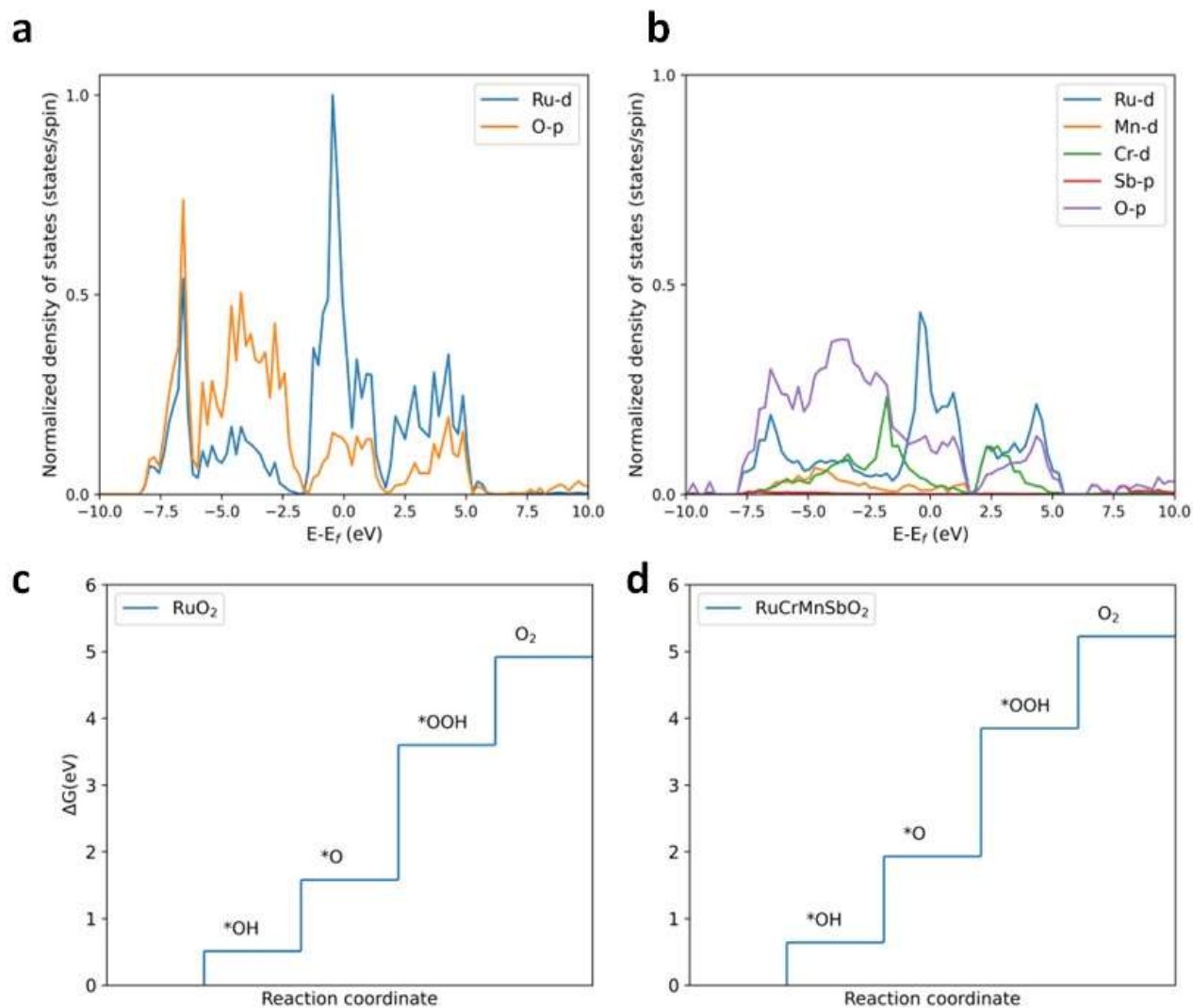


Fig. 5: Post-hoc DFT analysis of the best candidates

Figures (a, b) show DOS decomposed into elemental contributions and normalized to one for all the constituent elements for RuO₂ and C₁. The density of states for RuO₂ at fermi level is 38 states/(eV·spin) larger than 18 states/(eV·spin) in C₁ which is an indicator of better chemical bonding⁵⁷. Figures (c, d) show free energy diagrams for OER with both the catalysts (RuO₂ and RuCrMnSbO₂). In both cases, *OOH formation is the Rate Determining Step (RDS) with $E_{RuO_2} > E_{RuCrMnSbO_2}$ where E represents overpotential.

References:

1. Choudhary, K. *et al.* Accelerated Discovery of Efficient Solar Cell Materials Using Quantum and Machine-Learning Methods. *Chem. Mater.* **31**, 5900–5908 (2019).
2. Saidi, W. A., Shadid, W. & Vesper, G. Optimization of High-Entropy Alloy Catalyst for Ammonia Decomposition and Ammonia Synthesis. *J. Phys. Chem. Lett.* **12**, 5185–5192 (2021).
3. Kirman, J. *et al.* Machine-Learning-Accelerated Perovskite Crystallization. *Matter* **2**, 938–947 (2020).
4. Tao, Q., Xu, P., Li, M. & Lu, W. Machine learning for perovskite materials design and discovery. *npj Comput. Mater.* **2021 71 7**, 1–18 (2021).
5. Back, S., Tran, K. & Ulissi, Z. W. Discovery of Acid-Stable Oxygen Evolution Catalysts: High-Throughput Computational Screening of Equimolar Bimetallic Oxides. *ACS Appl. Mater. Interfaces* **12**, 38256–38265 (2020).
6. Jain, A., Voznyy, O. & Sargent, E. H. High-Throughput Screening of Lead-Free Perovskite-like Materials for Optoelectronic Applications. *J. Phys. Chem. C* **121**, 7183–7187 (2017).
7. Ren, Z. *et al.* Inverse design of crystals using generalized invertible crystallographic representation. (2020).
8. Davies, D. W. *et al.* Computational Screening of All Stoichiometric Inorganic Materials. *Chem* (2016) doi:10.1016/j.chempr.2016.09.010.
9. Xie, T. & Grossman, J. C. Crystal Graph Convolutional Neural Networks for an Accurate and Interpretable Prediction of Material Properties. *Phys. Rev. Lett.* (2018) doi:10.1103/PhysRevLett.120.145301.
10. Chen, C., Ye, W., Zuo, Y., Zheng, C. & Ong, S. P. Graph Networks as a Universal Machine Learning Framework for Molecules and Crystals. *Chem. Mater.* (2019) doi:10.1021/acs.chemmater.9b01294.
11. Park, C. W. & Wolverton, C. Developing an improved crystal graph convolutional neural network framework for accelerated materials discovery. *Phys. Rev. Mater.* (2020) doi:10.1103/physrevmaterials.4.063801.
12. Isayev, O. *et al.* Universal fragment descriptors for predicting properties of inorganic crystals. *Nature Communications* (2017) doi:10.1038/ncomms15679.
13. Rosen, A. S. *et al.* Machine learning the quantum-chemical properties of metal–organic frameworks for accelerated materials discovery. *Matter* **4**, 1578–1597 (2021).
14. Noh, J. *et al.* Inverse Design of Solid-State Materials via a Continuous Representation. *Matter* **1**, 1370–1384 (2019).
15. Gómez-Bombarelli, R. *et al.* Automatic Chemical Design Using a Data-Driven Continuous Representation of Molecules. *ACS Cent. Sci.* **4**, 268–276 (2018).
16. Yao, Z. *et al.* Inverse design of nanoporous crystalline reticular materials with deep generative models. *Nat. Mach. Intell.* **2021 31 3**, 76–86 (2021).

17. Kim, B., Lee, S. & Kim, J. Inverse design of porous materials using artificial neural networks. *Sci. Adv.* **6**, eaax9324 (2020).
18. Dan, Y. *et al.* Generative adversarial networks (GAN) based efficient sampling of chemical composition space for inverse design of inorganic materials. *npj Comput. Mater.* **6**, 1–7 (2020).
19. Guimaraes, G. *et al.* Objective-Reinforced Generative Adversarial Networks (ORGAN) for Sequence Generation Models.
20. Sanchez-Lengeling, B., Outeiral, C., Guimaraes, G. L. & Aspuru-Guzik, A. Optimizing distributions over molecular space. An Objective-Reinforced Generative Adversarial Network for Inverse-design Chemistry (ORGANIC). (2017) doi:10.26434/CHEMRXIV.5309668.V3.
21. Reeves, S. *et al.* Assessing methods and obstacles in chemical space exploration. *Appl. AI Lett.* **1**, e17 (2020).
22. Thiede, L. A., Krenn, M., Nigam, A. & Aspuru-Guzik, A. Curiosity in exploring chemical space: Intrinsic rewards for deep molecular reinforcement learning. (2020).
23. van de Walle, A. Multicomponent multisublattice alloys, nonconfigurational entropy and other additions to the Alloy Theoretic Automated Toolkit. *Calphad Comput. Coupling Phase Diagrams Thermochem.* **33**, 266–278 (2009).
24. Blum, V. & Zunger, A. Mixed-basis cluster expansion for thermodynamics of bcc alloys. *Phys. Rev. B - Condens. Matter Mater. Phys.* **70**, 155108 (2004).
25. Hiroshi Nakayama, Junpei Koyama, Noboru Yoneoka & Toshiyuki Miyazawa. Description: Third Generation Digital Annealer Technology. https://www.fujitsu.com/jp/documents/digitalannealer/researcharticles/DA_WP_EN_20210922.pdf (2021).
26. Hong, S., Miasnikof, P., Kwon, R. & Lawryshyn, Y. Market Graph Clustering Via QUBO and Digital Annealing. *J. Risk Financ. Manag.* **14**, 34 (2020).
27. Naghsh, Z., Javad-Kalbasi, M. & Valaee, S. Digitally Annealed Solution for the Maximum Clique Problem with Critical Application in Cellular V2X. in *IEEE International Conference on Communications* vols 2019-May (Institute of Electrical and Electronics Engineers Inc., 2019).
28. van de Walle, A., Asta, M. & Ceder, G. The Alloy Theoretic Automated Toolkit: A User Guide. *Calphad Comput. Coupling Phase Diagrams Thermochem.* **26**, 539–553 (2002).
29. Blum, V., Hart, G. L. W., Walorski, M. J. & Zunger, A. Using genetic algorithms to map first-principles results to model Hamiltonians: Application to the generalized Ising model for alloys. *Phys. Rev. B - Condens. Matter Mater. Phys.* (2005) doi:10.1103/PhysRevB.72.165113.
30. Paufler, P. F. Ducastelle. Order and Phase Stability in Alloys. (Cohesion and Structure Vol. 3). North-Holland/Elsevier Science Publishers, Amsterdam 1991. 511 p. US \$ 151./Dfl. 295.00. ISBN 0-444-86973-5. The book is available either from the Amsterdam address or from Elsevier Sc. Publ. New York. *Cryst. Res. Technol.* **27**, 874–874 (1992).
31. Sanchez, J. M., Ducastelle, F. & Gratias, D. Generalized cluster description of multicomponent systems. *Phys. A Stat. Mech. its Appl.* **128**, 334–350 (1984).
32. Li, C., Nilson, T., Cao, L. & Mueller, T. Predicting activation energies for vacancy-mediated

- diffusion in alloys using a transition-state cluster expansion. *Phys. Rev. Mater.* **5**, 013803 (2021).
33. Mueller, T. & Ceder, G. Bayesian approach to cluster expansions. *Phys. Rev. B - Condens. Matter Mater. Phys.* **80**, 024103 (2009).
 34. Ozoliņš, V., Wolverton, C. & Zunger, A. Cu-Au, Ag-Au, Cu-Ag, and Ni-Au intermetallics: First-principles study of temperature-composition phase diagrams and structures. *Phys. Rev. B - Condens. Matter Mater. Phys.* **57**, 6427–6443 (1998).
 35. Blum, V. *et al.* *Hands-On Tutorial on Cluster Expansion Modeling of configurational energetics Manuscript for Exercise Problems Adapted from a tutorial originally prepared by.* (2014).
 36. Babbush, R., Perdomo-Ortiz, A., O’gorman, B., Macready, W. & Aspuru-Guzik, A. *Construction of Energy Functions for Lattice Heteropolymer Models: A Case Study in Constraint Satisfaction Programming and Adiabatic Quantum Optimization.* (2013).
 37. Kim, D. W., Park, Y. J., Moon, J. W., Ryi, S. K. & Park, J. S. The effect of Cu reflow on the Pd–Cu–Ni ternary alloy membrane fabrication for infinite hydrogen separation. *Thin Solid Films* **516**, 3036–3044 (2008).
 38. Feng, Y. *et al.* Surface-modulated palladium-nickel icosahedra as high-performance non-platinum oxygen reduction electrocatalysts. *Sci. Adv.* **4**, eaap8817 (2018).
 39. Lin, Y. *et al.* Chromium-ruthenium oxide solid solution electrocatalyst for highly efficient oxygen evolution reaction in acidic media. *Nat. Commun.* **10**, 1–13 (2019).
 40. Teeriniemi, J., Taskinen, P. & Laasonen, K. First-principles investigation of the Cu–Ni, Cu–Pd, and Ni–Pd binary alloy systems. *Intermetallics* **57**, 41–50 (2015).
 41. Shi, Z., Wang, X., Ge, J., Liu, C. & Xing, W. Fundamental understanding of the acidic oxygen evolution reaction: Mechanism study and state-of-the-art catalysts. *Nanoscale* vol. 12 13249–13275 (2020).
 42. Hu, C., Zhang, L. & Gong, J. Recent progress made in the mechanism comprehension and design of electrocatalysts for alkaline water splitting. *Energy Environ. Sci.* **12**, 2620–2645 (2019).
 43. Seitz, L. C. *et al.* A highly active and stable IrO_x/SrIrO₃ catalyst for the Oxygen evolution reaction. *Science (80-)*. **353**, 1011–1014 (2016).
 44. Yang, L. *et al.* Efficient oxygen evolution electrocatalysis in acid by a perovskite with face-sharing IrO₆ octahedral dimers. *Nat. Commun.* **9**, 1–9 (2018).
 45. Back, S., Tran, K. & Ulissi, Z. W. Discovery of Acid-Stable Oxygen Evolution Catalysts: High-Throughput Computational Screening of Equimolar Bimetallic Oxides. *ACS Appl. Mater. Interfaces* **12**, 38256–38265 (2020).
 46. Zhang, B. *et al.* High-valence metals improve oxygen evolution reaction performance by modulating 3d metal oxidation cycle energetics. *Nat. Catal.* **3**, 985–992 (2020).
 47. Gou, W., Zhang, M., Zou, Y., Zhou, X. & Qu, Y. Iridium–Chromium Oxide Nanowires as Highly Performed OER Catalysts in Acidic Media. *ChemCatChem* **11**, 6008–6014 (2019).
 48. Dionigi, F. & Strasser, P. NiFe-Based (Oxy)hydroxide Catalysts for Oxygen Evolution Reaction in Non-Acidic Electrolytes. *Advanced Energy Materials* vol. 6 1600621 (2016).

49. Li, L., Wang, P., Shao, Q. & Huang, X. Recent Progress in Advanced Electrocatalyst Design for Acidic Oxygen Evolution Reaction. *Advanced Materials* 2004243 (2021) doi:10.1002/adma.202004243.
50. Hammer, B. & Nørskov, J. K. Theoretical surface science and catalysis—calculations and concepts. *Adv. Catal.* **45**, 71–129 (2000).
51. Hammer, B. & Nørskov, J. K. Why gold is the noblest of all the metals. *Nature* **376**, 238–240 (1995).
52. Hammer, B. & Nørskov, J. K. Electronic factors determining the reactivity of metal surfaces. *Surf. Sci.* **343**, 211–220 (1995).
53. Chemical Bonding at Surfaces and Interfaces - 1st Edition. <https://www.elsevier.com/books/chemical-bonding-at-surfaces-and-interfaces/nilsson/978-0-444-52837-7>.
54. Liu, J. *et al.* Progress and Challenges Toward the Rational Design of Oxygen Electrocatalysts Based on a Descriptor Approach. *Adv. Sci.* **7**, 1901614 (2020).
55. Zhang, B. *et al.* Homogeneously dispersed, multimetal oxygen-evolving catalysts. *Science* **352**, 333–338 (2016).
56. Wen, Y. *et al.* Stabilizing Highly Active Ru Sites by Suppressing Lattice Oxygen Participation in Acidic Water Oxidation. *J. Am. Chem. Soc.* **143**, 6482–6490 (2021).
57. Sorantin, P. I. & Schwarz, K. Chemical bonding in rutile-type compounds. *Inorg. Chem.* **31**, 567–576 (2002).
58. Yuge, K. Modeling configurational energetics on multiple lattices through extended cluster expansion. *Phys. Rev. B - Condens. Matter Mater. Phys.* **85**, 144105 (2012).
59. Jain, A. *et al.* Commentary: The materials project: A materials genome approach to accelerating materials innovation. *APL Materials* vol. 1 011002 (2013).
60. Troppenz, M., Rigamonti, S. & Draxl, C. Predicting Ground-State Configurations and Electronic Properties of the Thermoelectric Clathrates Ba₈Al_xSi_{46-x} and Sr₈Al_xSi_{46-x}. *Chem. Mater.* **29**, 2414–2424 (2017).
61. Rigamonti, S. & Draxl, C. *CELL-a python package for cluster expansion with a focus on complex alloys.* (2019).
62. Perdew, J. P., Burke, K. & Ernzerhof, M. Generalized gradient approximation made simple. *Phys. Rev. Lett.* (1996) doi:10.1103/PhysRevLett.77.3865.
63. Zhang, B. *et al.* Homogeneously dispersed multimetal oxygen-evolving catalysts [Supplementary Material]. *Science (80-.).* **352**, 333–337 (2016).

Acknowledgements:

This work was financially supported by Fujitsu Ltd. and Fujitsu Consulting (Canada) Inc. We thank Fujitsu for their generous access to the Digital Annealer where all the annealing operations and optimizations

were performed. All the DFT calculations were performed on the Compute Canada's Niagara supercomputing cluster. We thank Mr. Hidetoshi Matsumura (Fujitsu Consulting (Canada) Inc.) for the constructive feedback and discussions. The experimental work was supported financially by the Natural Sciences and Engineering Research Council (NSERC) of Canada, Vanier Canada Graduate Scholarship. Electron microscopy was conducted at the Ontario Center for the Characterization of Advanced Materials (OCCAM).

Competing interests:

The authors declare no competing interests.